Enhanced resolution capability of SWOT sea surface height measurements and its application in monitoring ocean dynamics variability

Yong Wang[1]· Shengjun Zhang[1] *·Yongjun Jia[2]

1. School of Resources and Civil Engineering, Northeastern University, Shenyang, China.

2. National Satellite Ocean Application Service (NSOAS), Beijing 100081, China

Correspondence to: Shengjun Zhang (zhangshengjun@whu.edu.cn)

1 **Abstract.**

2 The wavenumber spectrum of sea surface height along ground profiles is commonly determined to
3 quantify the magnitude of detectable ocean dynamic features by altimetry missions. In this paper,
4 wavenumber spectral were calculated and compared for HY2B, Saral/AltiKa, Sentinel-3A, and SWOT.
5 The wavenumber power spectral density(PSD) of sea surface height (SSH) was averaged using weighted
6 methods across multiple along tracks within defined boxes. The deduced resolution capabilities were
7 also compared and analyzed, evaluated using the relevant definition of one-dimensional mesoscale
8 resolution capability. We verified that the latest wide-swath SWOT mission offers significantly improved
9 measurements. For example, in the vicinity of Kuroshio, the one-dimensional mesoscale resolution of
10 SWOT is about 25 kilometers, twice the resolution capability of conventional satellites. In addition, the
11 quality of measurements declined obviously over regions where the eddy kinetic energy gets larger.
12 Finally, a global analysis of ocean dynamics variability scales was conducted based on two cycles of
13 SWOT data using reciprocal power spectral analysis. The results showed significant geographic and
14 temporal variations in the ocean dynamics variability scales, which are mainly relative to sea state
15 variability. The regions with large scales of ocean dynamics variability are concentrated in oceans with
16 strong currents and unstable sea states, such as the Kuroshio Current, the Gulf Stream, and the Antarctic
17 Circumpolar Current. In addition, the scale of ocean dynamics variability is not necessarily large where
18 eddy kinetic energy is large, such as the equator and the northwest Indian Ocean current area. Ocean
19 dynamics variability also varies across seasons.

1. Introduction

21 In recent decades, a series of satellites with altimeters onboard were launched, enabling continuous
22 monitoring of sea surface height (SSH) information on a global scale. These developments also led to a
23 better understanding of multi-scale dynamical phenomena (e.g., El Niño, Rossby waves, mesoscale
24 eddies, etc.) in the ocean surface (Boas et al., 2022). Within this, mesoscale dynamics are connected
25 through interactions with large-scale oceans (Smith et al., 2001). At the same time, mesoscale eddies
26 generate finer mesoscale and sub-mesoscale motions through small-scale frontal formations at the sea
27 surface (Lapeyre et al., 2008). Driven by different mechanisms of quasi-geostrophic (QG) dynamics,
28 sub-mesoscale activity can also reverse cascade these energies from the sub-mesoscale to the mesoscale
29 energy (Cao et al., 2021; Qiu et al.,2022). Processes at these spatial scales, through kinetic energy
30 cascades and energy dissipation, are essential for determining the upper ocean energy transfer.
31 (McWilliams et al., 2016; Rocha et al., 2016).

32 Multi-satellite merged products have been widely applied in oceanography, such as detecting and
33 tracking mesoscale eddies(Samelson et al., 2014; Yi et al., 2014; Chen et al.,2019). However, the optimal
34 interpolation algorithm heavily smoothed the spatial scales below 200 km during the product
35 manufacturing process, preserving only a limited portion of the small-wavelength signals (Dufau et al.,
36 2016). Therefore, those merged products are only suitable for observing mesoscale ocean dynamics at
37 wavelengths exceeding 150-200 km. (Vergara et al., 2023; Samelson et al., 2014; Boas et al., 2022; Dufau
38 et al., 2016).It is impractical to use traditional satellite altimetry missions to study the two-dimensional
39 sub-mesoscale dynamics of the ocean. The Surface Water and Ocean Topography (SWOT) satellite,
40 successfully launched by NASA in December 2022, observes SSH through a 50-km strip on either side
41 of the satellite nadir. It is expected to be able to resolve two-dimensional SSH variability structures at
42 wavelengths down to 15 km (Boas et al., 2022; Chelton et al., 2019). This will also dramatically enhance

43   our understanding of upper ocean dynamical processes in the mesoscale to sub-mesoscale wavelength
44   range (15-200km).

45   Before SWOT, sub-mesoscale dynamics were unresolved by AVISO's merged products or by most
46   global eddy-resolved models. However, they can be partially captured by SSH observations along
47   satellite profiles. Along-track altimeter data offers higher spatial resolution than merged data. It is capable
48   of sustained, repeated sampling of the global oceans so that the variability of SSH can be analyzed and
49   statistically assessed. In particular, the estimation of the power spectral density(PSD) of its SSH
50   wavenumber can be used to analyze the energy and cascade(Dufau et al., 2016; Le Traon et al., 2008; Xu
51   et al., 2011, 2012). Based on the hypothesis of geostrophic balance, energy conservation, and potential
52   vortex conservation, the wavenumber spectrum of SSH lies between the quasi-geostrophic (QG)
53   turbulence theory and the surface quasi-geostrophic (SQG) turbulence theory (Xu et al., 2012; Qiu et al.,
54   2018; Chereskin et al., 2019; Callies et al., 2011). The theory predicts that the spectral slope of the
55   wavenumber (K) varies from k^{-5} to $k^{-\frac{11}{3}}$ in the mesoscale to sub-mesoscale scale range. Xu Y et al.
56   (2012) first utilized Jason1 data and accounted for the effect of noise to perform chunk statistics on the
57   PSD of global SSH wavenumber. They found that in the energy core regions of major ocean currents
58   (e.g., Kuroshio, Gulf Stream, Antarctic Circumpolar Current, Brazilian Warm Current, etc.), their slopes
59   can be observed to be between the QG turbulence theory and the SQG turbulence theory. Besides these
60   high kinetic energy regions, the slopes in the temperate and tropical zones are significantly lower than
61   $k^{-\frac{11}{3}}$, which they attribute mainly to the influence of non-geostrophic dynamics.

62   Dufau et al.(2016) proposed a method defined as the one-dimensional mesoscale resolution
63   capability of altimetry satellites. The slope is determined by fitting the 90-280 km wavenumber spectrum
64   and using 25 km below as the noise constant. The intersection between these two is defined as the one-
65   dimensional mesoscale resolution capability. There are significant differences in resolution capability
66   attributable to varying noise levels of altimeters in different frequency bands and modes. The Jason2 uses
67   Ku-band low-resolution mode (LRM), which typically only resolves wavelengths of about 70 km
68   (Vergara O et al., 2019). The Saral/AltiKa uses a 40 HZ Ka-band transmitting frequency, a wider
69   bandwidth, and a higher pulse repetition frequency, resulting in lower noise levels than Ku-band LRM
70   altimeters(Raynal et al., 2018). Thus, it exhibits a higher one-dimensional mesoscale resolution
71   capability than the Jason satellite (Dufau et al., 2016). Another altimeter uses the Ku-band synthetic
72   aperture radar (SAR) mode, which achieves lower noise compared to Jason2 and Saral/AltiKa. (Vergara
73   O et al., 2019). Its true resolution capability is also better than Jason2's LRM mode and the Saral/AltiKa
74   satellite (Raynal et al., 2018). The latest SWOT satellite uses a Ka-band radar interferometer (KaRIN),
75   increasing spatial resolution along the track to 2 km and thereby greatly enhancing our understanding of
76   sub-mesoscale dynamics (Callies et al., 2019). Accordingly, this paper provides an updated analysis of
77   the global SSH spectral slope using different types of altimetry missions. The method of Dufau et al.
78   (2016) was adopted and improved to statistically analyze the one-dimensional resolution capability of
79   altimetry satellites with different modes and frequencies to further validate the enhancement brought by
80   SWOT satellites. Finally, the dynamical scales of the global ocean are analyzed through SWOT data.

81   This paper is structured as follows. In section 2, we describe the altimetry dataset used and a specific
82   description of the method improvement. In section 3, we statistically assess the noise levels of altimetry
83   satellites of different modes and frequencies and the global one-dimensional mesoscale resolution
84   capability. Section 4 defines a parameter using reciprocal power spectral analysis and analyzes global

85 ocean dynamics variability at the mesoscale and sub-mesoscale using SWOT data. Finally, we summarize

86 the enhancement brought about by the SWOT satellite.

2. Datasets and Methodology

2.1 SSH Datasets

89 Along-track SSH data from four altimetry missions (HY2B, Saral/AltiKa, S3A, SWOT) using

90 different techniques are analyzed on a global ocean scale. SWOT mission is two-dimensional data,

91 therefore we split each two-dimensional piece of data into multiple pieces of data along the track. For

92 Section 3, we only selected data from October to November 2023 for analysis due to the large amount of

93 SWOT data. To compare the resolution capability of the different techniques of altimetry as well as to

94 validate the enhancement of resolution capability brought about by SWOT's KaRIn. For Section 4, data

95 from 8 cycles of the SWOT mission are used. For the first three missions, we select only 1hz data; for

96 SWOT data, we choose the cross-corrected oceanic Level 3 product. The details of the four missions are

97 described below.

98 The HY2B satellite mission Level 2 products are all released by the National Satellite Ocean

99 Application Service Center of China (NSOAS, http://www.nsoas.gov.cn/), with a repeat cycle of 14 days.

100 The satellite mainly carries dual-frequency radar altimeter (Ku and C bands), and the Ku band is mainly

101 used for distance measurement. HY-2B satellite radar altimeter secondary products include Interim

102 geophysical data records (IGDR), Sensor geophysical data records (SGDR), and GDR. IGDR is an

103 uncorrected data product obtained using Medium precision orbit ephemeride (MOE) orbit fix data,

104 waveform reconstruction, etc. GDR is an uncorrected data product obtained using Precise orbit

105 ephemeride (POE) orbit fix data, waveform reconstruction, etc. GDR is an uncorrected data product

106 obtained by using Precise orbit ephemeride (POE) orbit fix data. GDR is a fully corrected data product

107 obtained using Precise orbit ephemeride (POE) orbit data, waveform reconstruction, etc. SGDR is the

108 same as IGDR and GDR, but the difference lies in including waveform data. In this paper, we use the

109 SGDR data of HY2B with periods 129 to 131.

110 The SARAL/AltiKa satellite was launched as a collaboration between the Indian Space Research

111 Organisation (ISRO) and the French National Centre for Space Studies (CNES) (Verron J et al., 2015),

112 with a repetitive period of 35 days. Using the Ka-band reduces the footprint, increases the pulse repetition

113 frequency, and provides a higher accuracy of distance estimation at 40hz even compared to the 20hz

114 sampling of the classical Ku-band altimeter (Quartly et al., 2015). In ocean observations, it improves the

115 accuracy of SSH, especially for ocean mesoscale observations (Verron et al., 2021). The advantages of

116 the Ka-band are reduced ionospheric effects, smaller footprint, better horizontal resolution, and higher

117 vertical resolution. A disadvantage of the Ka-band is the attenuation in rainy conditions due to

118 water/water vapor and the resultant loss of data The final choice was the SARAL/Altair band. Finally, a

119 portion of the SARAL/AltiKa data for cycles 175 and 176 was selected.

120 The Sentinel-3A (S3A) satellite carries the SRAL altimeter for distance measurements, which is

121 processed using delayed Doppler processing designed to achieve significantly higher signal-to-noise

122 ratios (Heslop et al., 2017). The main frequency used for distance measurements is Ku-band (13.575

123 GHz with a bandwidth of 350 MHz) and C-band frequency (5.41 GHz with a bandwidth of 320 MHz) is

124 used for ionospheric correction. There are two radar modes, Low Resolution Mode (LRM) and Synthetic

125 Aperture Radar (SAR) mode. The SRAL mission on S3A always operates in high-resolution mode (often

126   referred to as SAR mode). The repetition period of the S3A sun-synchronous orbit was 27 days. Finally,
127   the data for the 104 and 105-cycle portions of S3A were selected.

128   The SWOT satellite was launched in December 2022. It provides the first two-dimensional high-
129   resolution measurement of water height from space using two SAR antennas separated by a 10-meter
130   mast for interferometry in orbit. SWOT adopts Ka-band radar interferometry (KaRIn) for measurements
131   over a narrow strip of 120 kilometers (20-kilometer gap of sub-stellar points sampled at coarse resolution
132   along the centerline by a conventional altimeter). SWOT carries s Ka-band radar interferometer with
133   azimuthal resolution of 2.5 m and distance resolution of 10-70 m. The pixel sizes of a few tens of meters
134   are much smaller than the pulse-limited footprint area (~10 km) of conventional altimeters, and the high
135   resolution of the radar system permits averaging over a large number of pixels to minimize noise and
136   still resolve small-scale signals (Fu et al., 2024). In this paper, SWOT's latest cross-corrected L3 product
137   is used. Selected data from SWOT's ocean product for cycles 1 through 14 are selected for this paper.
138   Data for the latter three missions are available for download from the AVISO website
139   (https://www.aviso.altimetry.fr).

140   The along-orbit SSH (HY2B, SARAL/AltiKa, S3A) observations were kept at their original 1hz
141   observation positions at intervals of about 7km and corrected for all instrumental, environmental, and
142   geophysical corrections. The SWOT mission selects data in the along-orbit direction with an interval of
143   2 km. All missions follow (Xu et al., 2011, 2012; Dufau et al., 2016) in calculating SSH anomalies by
144   subtracting from the along-orbit SSH measurements the Mean Sea Surface Model (MSS)
145   CNES_CLS_2015, which is the time-varying portion of the SSH.

2.2 Methodology

147   Wavenumber spectral analysis is a common method to study the characteristics of a signal or system
148   within the frequency domain. The spectral signal is obtained by sampling the signal in the time domain
149   and Fourier transforming it, and then sampling it in the frequency domain to obtain a frequency domain
150   signal. Wavenumber represents the number of wavelengths per unit distance. The wavenumber spectrum
151   indirectly reflects the energy distribution in the ocean at different spatial scales. The shape and
152   characteristics of the spectrum can provide important information about the underlying physical
153   processes(He et al., 2024).

154   We calculated the SSH anomalous wavenumber power spectral density (PSD) for each mission
155   globally in a 10°x10° box. The specific preprocessing steps for calculating the PSD for each along-track
156   SSH within a box are similar to those described by Dufau et al.(2016). For each $10° \times 10°$ box, we
157   departed from the previous method of averaging all individual PSD to obtain an average PSD. The global
158   PSD has a resolution of $2° \times 2°$, however, each grid point is analyzed within a $10° \times 10°$ box to compute
159   the PSD. Averaging over a $10° \times 10°$ area would diminish the signal in regions with higher mesoscale
160   energies, as well as affect the assessment of areas with lower energies. Consequently, we follow the
161   method in Appendix A to calculate the distance between each SSH along the track and the reference point.
162   Then, the weight of the PSD for each SSH in the region is assigned based on this distance. The method
163   of weighted averaging can reduce the error in calculating the PSD of the grid points and preserve the
164   signal of the grid point location as much as possible so that the calculation results can be more credible.
165   Finally, using the PSD after weighted averaging, three parameters were derived using the method of
166   Dufau et al. (2016): the 1 Hz SSH error level (SWOT is the 2 km sampling rate along the track), the SSH
167   spectral slope in the mesoscale bands, and their intersections, expressed as wavelengths, referred to as
168   the "one-dimensional mesoscale resolution capability".

169   For wavelengths below 25 km for the first three missions, the 1 Hz SSH error level was estimated

170   by fitting a level to the spectrally flat noise levels present in the PSD maps (Figure. 1). SWOT error

171   levels were estimated by fitting a level to noise levels below 15 km, adopting the results of Chelton et al.

172   (2019) on the assessment of noise levels in SWOT. These arise primarily from inhomogeneities in the

173   radar backscatter coefficient within the altimeter footprint, resulting in inaccuracies in SSH estimates

174   and generating greater spectral noise.

175   The PSD of SSH was estimated first by removing the estimated constant error level below and

176   subsequently performing a linear slope estimation. Diverse methods for calculating the Power Spectral

177   Density (PSD) can result in minor discrepancies in the slope range(Vergara et al., 2019) Additionally,

178   data sampled at varying frequencies may also engender subtle variances in the estimated PSD slope range.

179   Hence, for the first three conventional missions, we chose wavelengths in the range of 70-250 km and

180   fitted the slope of the PSD by least squares. The lower limit was chosen to ensure a robust slope estimate,

181   as the shape of the PSD exhibits greater variability below this limit (e.g., Figure. 1). The 70-km

182   wavelength exceeds the shorter wavelengths affected by altimeter noise. For the SWOT mission, its

183   cross-correction process filters out some noise, resulting in a spectral profile that continually drops, as

184   shown in Figure 1. Due to the presence of many sub-mesoscale phenomena at 15-40km, such as internal

185   waves and tides, etc(Boas et al., 2022). Therefore, a wavelength of 40-125 km was selected for

186   calculating the PSD slope for the SWOT mission. The intersection where the error level and the spectral

187   slope intersect is set to the wavelength at which the PSD of the minimum scale signal is equal to the error

188   level. This defines the one-dimensional mesoscale resolution capability. We will also use this parameter

189   to compare the resolution capability of different modes of altimetry satellite missions in Section 3 to

190   assess the improvement in mesoscale resolution capability provided by the SWOT satellite.
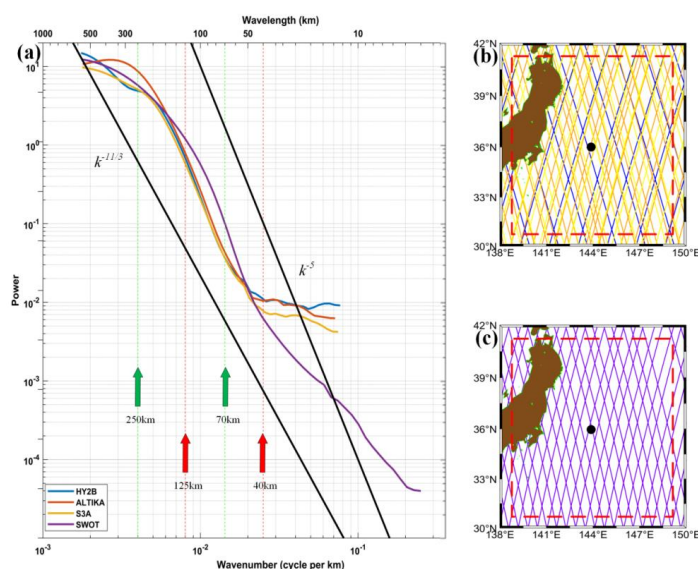
191

192   **Figure. 1 a. Along-track SSH averaged PSDs for HY2B, SARAL/ALTIKA, S3A, and SWOT**

193   **within the Kuroshio Extension (green arrows represent the range over which PSD slopes were**

194   **computed for conventional satellites, red arrows represent the range over which PSD slopes were**

195   **computed for SWOT satellites, and the black solid lines show the spectral slopes which correspond**

196 to k^{-5} and $k^{-11/3}$). **b. The tracks of the first three satellites within the Kuroshio region distribution**
197 **map c. Distribution map of SWOT satellite tracks within the Kuroshio region (only two along-**
198 **track data were selected for each pass). Red dashed lines represent the range over which the mean**
199 **PSD was computed.**

3. Global resolution capability of altimetry satellites

201   The global maps of SSH spectral slopes from October to November 2023 for the four different
202 model altimetry missions are almost identical (Figure. 2) . They are in general agreement with the global
203 map of slopes averaged over longer periods by Dufau et al.(2016) and Xu et al.(2012). The highest slope
204 distributions for each altimetry mission were observed in major ocean current regions, including the
205 Kuroshio, Gulf Stream, Antarctic Circumpolar Current, Brazilian Warm Current, and the North Indian
206 Ocean Current. The spectral slopes in these regions are all close to $k^{-4.2}$ or even higher, which is consistent
207 with the theoretical predictions from SQG and QG theories. The slopes are lower at lower latitudes,
208 typically below $k^{-2.1}$. Dufau et al. (2016) pointed out that the calculated PSD shows an important energy
209 peak near the 140 km wavelength at low latitudes. These peaks correspond to residual tidal signals
210 affecting the altimeter's SSH measurements, which are of varying strengths but may be hidden at mid-
211 latitudes by the higher geostrophic energy occurring at similar wavelengths. These peaks may be related
212 to errors in the positive pressure tidal correction. This may be due to uncorrected oblique pressure tides
213 in the altimeter's SSH measurements (Richman et al.2012). Another explanation is that the geostrophic
214 equilibrium motions (i.e., mesoscale eddies) in these regions are lower than those of Kinetic Energy (KE)
215 levels (i.e., internal waves). Thus, the latter would mask the energy levels associated with mesoscale
216 eddies (Tchilibou et al.,2018). This explains why satellites altimetry observed relatively small spectral
217 slopes at these latitudes. Vergara et al. (2019) combined spectral slopes with local stratification and
218 Rossby number, and used variable wavelength ranges to fit the slopes of the spectra. However, for this
219 paper, we focus on verifying the improvement brought by SWOT compared to other mission satellites.
220 Therefore, for the one-dimensional mesoscale resolution capability of different altimetry missions, we
221 compare and analyze only the mid-latitude regions where energy levels are higher.
222   We observe that the spectral slopes of SWOT are consistently higher than the results of the other
223 three missions. This may be related to the fact that the noise levels of HY2B, ALTIKA, and S3A hide the
224 ocean variability at a wavelength of about 70 km and will result in a smaller slope. It is also possible that
225 slight differences in the slopes arise from varying sampling rates, but the global map's distribution pattern
226 is essentially consistent. Although our calculated spectral slopes for the one month are similar to the
227 results of previous studies. However, there are still slight differences in the results due to differences in
228 the method of calculation, data processing, and the period of the study. In fact, several studies have
229 demonstrated that SSH spectral slopes exhibit seasonal variability. For example, in regions such as the
230 Kuroshio, the Gulf Stream, and the Pacific Northwest, the spectral slopes are stronger in summer and fall
231 and weaker in spring versus winter (Dufau et al.,2016; Vergara et al., 2019). The fact that our data were
232 chosen in October may explain why the spectral slopes calculated in this paper are slightly larger.

10.5194/egusphere-2024-3005
2024-10-02
Author(s) 2024. CC BY 4.0 License.

233
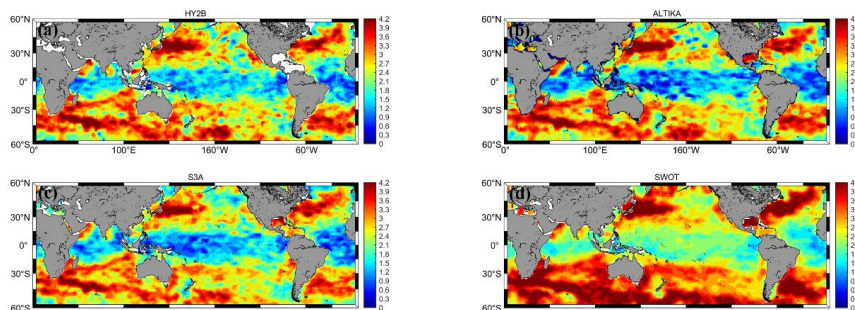
Figure. 2 Global slope maps for different satellites ((a) HY2B, (b) SARAL/ALTIKA, (c) S3A, (d) SWOT)

Figure. 3 depicts the spatial distribution of altimeter error levels over the global ocean for the four altimetry missions HY2B, SARAL/ALTIKA, S3A, and SWOT. As can be seen from Figure 3, HY2B uses the highest noise LRM mode in the Ku-band. The Ka-band used by SARAL/Altika demonstrates a significant reduction in the altimeter noise level. However, for the data from the period studied in this paper, it is clear that the trajectories for a particular period are all affected and span a wide range. This variability suggests a potential error in one of the satellite's corrections. Additionally, the error of the Ku-band SAR mode altimeter on the S3A satellite has shown significant improvement over the previous two modes. The error magnitude of the Ka-band interferometric mode on the latest SWOT satellite has been reduced by over 70 times compared to traditional satellites. Comparing Figure. 3 with Figure. 4 reveals that, regardless of the altimetry mission type, all exhibit similar distribution patterns, with higher altimeter noise in regions of greater eddy kinetic energy. This results in an increased level of altimeter error below 25km (15km). It is necessary to upgrade the technology in the future or use appropriate algorithms to minimize the effect of this error.

249
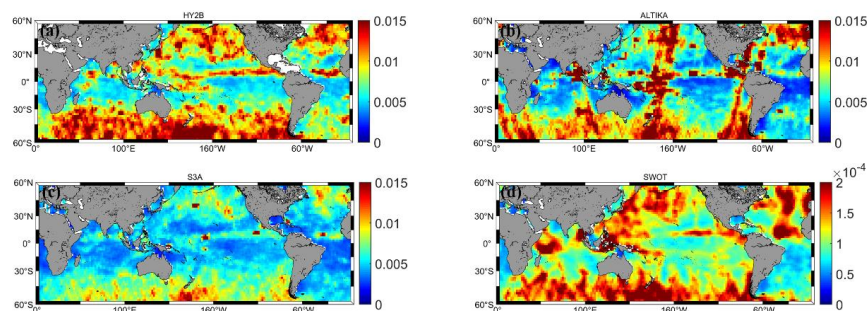
Figure. 3 Global noise levels of different satellites ((a) HY2B, (b) SARAL/ALTIKA, (c) S3A, (d) SWOT)
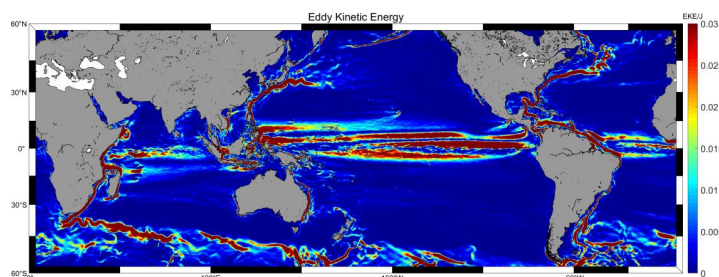
Figure. 4 Global distribution of eddy kinetic energy calculated by MDT2022

Based on the one-dimensional mesoscale resolution capability parameter defined by Dufau C et al. (2016), we plot the distribution of the globally observed minimum wavelengths for the four altimetry missions (Figure. 5). It is evident that the resolution wavelengths calculated for different altimetry missions and geographic locations are different. This variation is primarily due to differences in noise levels and PSD slopes. There may be some issues with the calculated slopes at low latitudes, so we compare the main ocean current region (Kuroshio). The resolution capability of the LRM mode in the Ku band of HY2B is relatively poor, around 60 km. t The SARAL/ALTIKA mission achieves resolution at wavelengths greater than 50 km. In contrast, the SAR mode of S3A achieves resolution at wavelengths slightly below 50 km. This result is consistent with the conclusions reached by Vergara et al. (2019) and Dufau et al.(2016). Although they studied the Jason1 satellite, both Jason1 and HY2B satellites use the Ku-band LRM mode for their measurements. Finally, as shown in Figure 5d compared to Figures 5a, b, and c, the KaRIN approach adopted by SWOT represents a significant advancement in resolution capability. The Kuroshio waters can be resolved at wavelengths around 20 km. This is mainly due to SWOT's significantly lower noise level and the higher range of wavenumbers where the peak slope occurs. This paper only compares the along-track resolution capability of different missions. The primary advantage of SWOT lies in its capability to conduct two-dimensional SSH observations, which will provide unprecedented insights into small-scale ocean features. Experiments have demonstrated that SWOT's along-track resolution capability has also been greatly improved, providing a solid foundation for utilizing two-dimensional SSH data to study ocean dynamics.
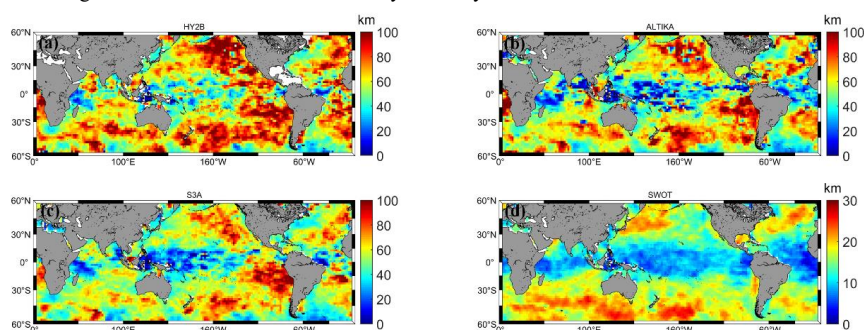
Figure. 5 Global resolved wavelengths for different satellites (a. HY2B, b. SARAL/ALTIKA, c. S3A, d. SWOT)

4. Global analyses of ocean-scale changes

We confirmed in the previous section the great enhancement brought by SWOT. This section focuses on the study and analysis of the dynamical scales in the ocean using data from different cycles of SWOT. Eight cycles were selected (from four different seasons), with two cycles grouped together for each experimental set. The four groups are cycles 13 and 14 representing spring, cycles 1 and 2 representing summer, cycles 4 and 5 representing autumn, and cycles 9 and 10 representing winter. Each of these datasets is calculated using the Appendix B reciprocal power spectra. Here, instead of utilizing the time-varying signal from the along-track SSH, we combine the ocean time-varying signal with the mean dynamical topography (MDT) to obtain the absolute dynamical topography (ADT). The specific subregional calculations are aligned with Appendix A.

In this paper, we use the method of Marks K M et al.(2016) to calculate the reciprocal power spectra of data from the same geographic location for two adjacent cycles and the corresponding spatial wavelengths when the mean square coherence reaches 0.5. The two cycles are separated by 21 days, and we define this parameter as the wavelength of the Ocean Dynamics Scale (ODS) that is observed at that geographic location on day 21. A map of ODS variability in the global ocean was constructed for four seasons according to the aforementioned standard (Figure 6). As can be seen from Figure 6, ODSs larger than 100 km are found mainly along the Western Boundary Current and the Antarctic Circumpolar Current. These regions exhibit high variability in mesoscale ocean dynamics and unstable oceanic phenomena. Notably, regions with higher eddy kinetic energy do not necessarily exhibit greater ODS variability. For example, in equatorial regions and the northwest Indian Ocean currents, both exhibit strong eddy kinetic energy (Figure 4). However, their ODS is relatively small during the period covered by the four experimental cycles, resulting in wavelengths that drive their variability being small, around 90 km.

There are different ODS variations in different geographic locations, and in the Western Boundary Current, the Gulf Stream has greater oceanic-scale variability than the Kuroshio region. In addition, the ODS variations at the same geographic locations vary seasonally. For example, at the confluence of the Oyashio and Kuroshio, wavelength variation is greater in spring compared to winter and smaller in summer compared to autumn. In contrast, in the western location of Australia, there is less variation in spring and winter and more variation in summer and fall. Except for the world's ocean current regions, the rest of the areas show minimal variation in ODS, generally below 60 km. The experimental results in this paper do not indicate the absence of small-scale changes in the region but rather calculate the largest-scale fluctuations in the area. The ODS of different ocean currents also differ, but it is important to note that the regional ODS of these ocean currents are generally greater than that of other locations. The parameter proposed in this paper can also be applied to SWOT data from one-day repeated cycles, which better represents ocean dynamics variability at temporal dynamic scales. It will also provide a novel reference point for future scientific research.
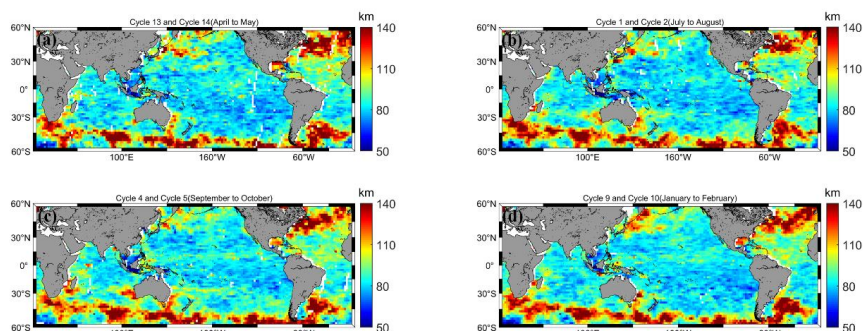
Figure. 6 Global Ocean mesoscale and sub-mesoscale size changes over four seasons

5. Conclusion

We assessed the capability of four different modes of satellite altimetry (Ku-band LRM, Ka-band LRM, Ku-band SAR mode, and Ka-band wide mode) for global ocean mesoscale resolution by comparing the PSD of their SSH along the track. In contrast to traditional averaging methods, this paper uses a weighted averaging method to calculate the mean value based on the distance between satellite orbits. This method provides a more accurate reflection of the noise level and resolution capability. The results show that the SWOT mission provides a significant improvement in along-track resolution capability compared to conventional one-dimensional altimetry satellites, especially in terms of noise level and one-dimensional mesoscale resolution. For example, in the vicinity of Kuroshio, the one-dimensional mesoscale resolution capability of SWOT is about 25km, which is about double the resolution capability of conventional satellites. In addition, we find that regions of high noise levels often correspond to regions of strong eddy kinetic energy. The higher the eddy kinetic energy, the relatively higher the noise level of the satellite.

Finally, by correlating eight cycles of SWOT data, we find significant ODS variations in the major ocean currents, including the Western Boundary Current and the Antarctic Circumpolar Current. It is noteworthy that ODS variations are not significant in the warm equatorial current region despite its high eddy energy. In addition, seasonal ODS variations were also observed for major ocean currents such as the Kuroshio and Gulf Stream, with the Kuroshio showing larger ODS variations in the spring and winter, and smaller ones in the summer and autumn. This study not only demonstrates the improvement in the resolution capability of SWOT along-track data but also lays the foundation for future studies of oceanic sub-mesoscale dynamics using two-dimensional SSH data from SWOT.

Data Availability Statement

The SWOT data, as well as the SARAL/AltiKa altimeter data, were provided by CNES (https://www.aviso.altimetry.fr/en/data.html), the Sentinel-3A altimeter data is provided by ESA (https://dataspace.copernicus.eu/) and can be publicly downloaded and used. The HY2B satellite mission Level 2 products are all released by the National Satellite Ocean Application Service Center of China (NSOAS, http://www.nsoas.gov.cn/). The MDT2022 can be downloaded from the AVISO website (https://www.aviso.altimetry.fr).

Conflict of interest The authors declare that they have no conflict of interest.

Author contributions

346   Wang Yong analyzed the data and wrote the manuscript draft; Zhang Shengjun and Jia Yongjun reviewed
347   and edited the manuscript.

Appendix A: Detailed description of the PSD averaging method for multiple tracks within the box

350   To avoid the effect of sea ice on SSH, we divided the globe (0°E ~ 360°E,60°N ~ 60°S) into 10,980
351   small 2° × 2° regions. The PSD at each grid point was calculated by extending the area to a 10° × 10°
352   box. To enhance the accuracy of the PSD at each grid point, we first calculated the distance D from the
353   SSH along the track to the grid point as follows.

354   The trajectories of the satellites in the 10° × 10° box resemble a parabola, as shown in Figure A1.
355   Therefore, we model the trajectory of each satellite using a binomial equation, as illustrated in Eq 1.

356   $$y_i = ax_i^2 + bx_i + c \qquad (1)$$

357   where i represents the number of compliant along-track SSHs in the box. x_i is the longitude
358   independent variable and y_i is the latitude dependent variable.

359   Assuming that the position of the grid points to be solved is (x_0, y_0), the distance D_i can be expressed
360   by Eq. 2.

361   $$D_i = \sqrt{(X_i - x_0)^2 + (Y_i - y_0)^2} \qquad (2)$$

362   Where (X_i, Y_i) is the position of the nearest point to the point to be sought in i trajectories. Therefore,
363   we only need to find the position of the nearest point to find out the shortest distance from the point to
364   be sought to the trajectory D_i. The relationship equation for distance minimization is established by
365   combining Eq1 and Eq 2.

366   $$f(x_i) = \sqrt{(x_i - x_0)^2 + (ax_i^2 + bx_i + c - y_0)^2} \qquad (3)$$

367   When the distance is minimum, the derivative of $f(x_i)$ should be zero at this point. Finally, it is
368   simplified to Eq 4.

369   $$x_i - x_0 + ax_i^2 + (bx_i + c - y_0)(2ax_i + b) = 0 \qquad (4)$$

370   The solution X_i of Eq. 4 needs to be computed using numerical iteration, and here we utilize
371   Newton's iterative method for the solution. Finally, the shortest distance D_i can be found.
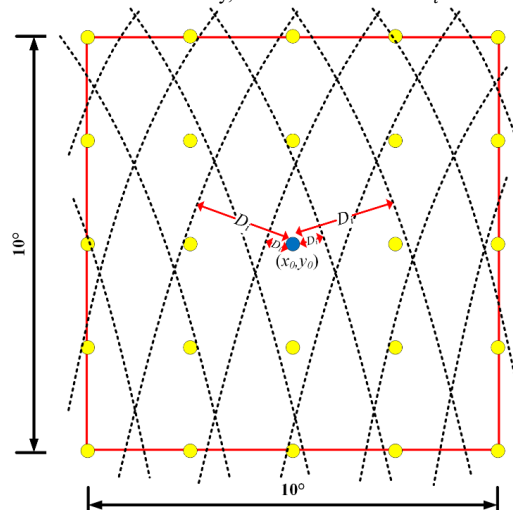
372

373 **Figure. A1 Schematic diagram of the satellite trajectory and the grid points to be solved,**
374 **where the blue points are the grid points to be solved, the yellow points are the other grid points,**
375 **the orange ones are the trajectories of the satellites, and the black lines represent the range of the**
376 **box.**

377

378 After calculating the distances of all the trajectories inside the box to the grid points to be solved,
379 we calculate the average PSD of the grid points using the Inverse Distance Weighting (IDW) method.
380 Since we are calculating for the global 2° × 2° small areas. Thus, the weights within a 1° extension of
381 the point to be sought in all four directions should be the same. To facilitate the calculation, we define
382 the weights in the form of a circle expanding outward. The specific distance variations are shown in
383 Figure. A2. All distances D_i are rounded to the right, e.g., the green region distances are all 1°. However,
384 the distances of the outermost black regions are all 5°, which is due to the smaller weights they occupy,
385 so they are set to the same distance. Finally, we then weighted and averaged the PSD values of the points
386 to be sought according to Eq 5.

387 $$P = \frac{\sum_{i=1}^{n} w_i P_i}{\sum_{i=1}^{n} w_i} \tag{5}$$

388 where w_i is $1/D_i$, D_i is the PSD of the i along-track SSH, and n represents the total number of all
389 tracks in the box. P is the average PSD value of the point to be sought.
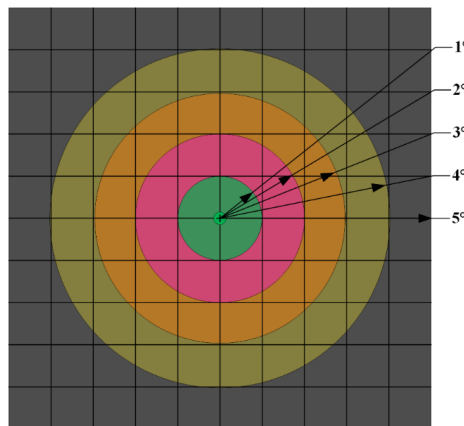
390
391 **Figure. A2 Weighted magnitude of the share of different distances**

392 **Appendix B: Mutual power spectral density analyses to**

393 **estimate ocean dynamics variability**

394 The coherence function and power spectrum reflect the degree of correlation between the signal and
395 the density of the power distribution with frequency. The purpose of power spectrum estimation is to
396 characterize the distribution of the frequency components of signals and stochastic processes based on a
397 finite data sequence. The coherence function determines the similarity between two repetitive period
398 signals and thus deduces the resolution capability. The frequency characteristics of two random signals
399 *x(t)* and *y(t)* relating to each other can be described by the reciprocal power spectral density as shown in
400 Eq 5. The mutual power spectral density and the mutual coherence function are also Fourier transforms,

401 and the phase difference obtained by calculating the mutual power spectral transformation can intuitively

402 reflect the degree of similarity between the two sequences in the frequency domain(ZHOU et al.,2024).

403 $$S_{xy}(f) = \int_{-\infty}^{+\infty} R_{xy}(\tau)e^{-j2\pi f\tau}d\tau \qquad (5)$$

404 where τ is the time difference and the coherence function of the signals *x(t)* and *y(t)* for two repetition

405 cycles is:

406 $$C_{xy}(\omega) = \frac{|P_{xy}(\omega)|^2}{P_{xx}(\omega)P_{yy}(\omega)} \qquad (6)$$

407 Where $P_{xy}(\omega)$ is the reciprocal power spectral density of *x(t)* and *y(t)*, and $P_{xx}(\omega)$ and $P_{yy}(\omega)$ are

408 the self-power spectral densities of *x(t)* and *y(t)* respectively. The coherence function can judge the degree

409 of similarity between two repetition cycle signals to infer resolution capability. Marks K M et al., (2016)

410 defined a criterion for judging the wavelength resolution of a geoid, i.e., the spatial wavelength

411 corresponding to a mean-square coherence of 0.5. We continue this defined criterion by using the degree

412 of similarity between the Absolute Dynamics Topography (ADT) of two repetitive cycles to determine

413 the scale variability occurring in the ocean, i.e., analyzing the wavelengths of near-time-varying scale

414 variability in the ocean.

415 Similar to Appendix A, we also divided the globe (0°E ~ 360°E,60°N ~ 60°S) into small 2° × 2°

416 regions, each region was analyzed with an outwardly expanding 10° × 10° box for the mutual power

417 spectrum. Since the along-track data of the two repetition cycles required strict alignment, interpolation

418 was required to fill in the missing data. If missing data occurs, to prevent the interpolation from affecting

419 the original ADT signal, we retained only the repetitive tracks with fewer than 15 missing data points.

420 Otherwise, the entire sample was rejected. To enhance the spatial coverage and maximize the number of

421 samples in each box, the along-track data were split into samples of approximately 560 km (280 data

422 points). From the mutual power spectrum, a new parameter was defined: the wavelength at which the

423 mean-square consistency reaches 0.5, indicating the extent of ocean dynamics scale variability at that

424 wavelength. Finally, all wavelengths within each box are weighted and averaged following the same

425 method as in Appendix A to yield the final global distribution. We utilize this parameter to evaluate

426 greater SWOT's ocean resolution capability in Section 4.

427 Reference

428 Boas A B V, Lenain L, Cornuelle B D, et al., 2022a. A Broadband View of the Sea Surface Height
429 Wavenumber Spectrum[J]. GEOPHYSICAL RESEARCH LETTERS, 49(4): e2021GL096699.

430 Callies J, Ferrari R, Klymak J M, et al., 2011. Seasonality in submesoscale turbulence[J]. Nature
431 Communications, 6: 6862.

432 Callies J, Wu W, 2019. Some Expectations for Submesoscale Sea Surface Height Variance Spectra[J].
433 JOURNAL OF PHYSICAL OCEANOGRAPHY, 49(9): 2271-2289.

434 Cao H, Fox-Kemper B, Jing Z, 2021. Submesoscale Eddies in the Upper Ocean of the Kuroshio
435 Extension from High-Resolution Simulation: Energy Budget[J]. JOURNAL OF PHYSICAL
436 OCEANOGRAPHY, 51(7): 2181-2201.

437 Chelton D B, Schlax M G, Samelson R M, et al., 2019. Prospects for future satellite estimation of small-
438 scale variability of ocean surface velocity and vorticity[J]. PROGRESS IN OCEANOGRAPHY,
439 173: 256-350.

440 Chen G, Han G, Yang X, 2019. On the intrinsic shape of oceanic eddies derived from satellite altimetry[J].
441 Remote Sensing of Environment, 228: 75-89.

Chereskin T K, Rocha C B, Gille S T, et al., 2019. Characterizing the Transition From Balanced to Unbalanced Motions in the Southern California Current[J]. JOURNAL OF GEOPHYSICAL RESEARCH-OCEANS, 124(3): 2088-2109.

Dufau C, Orsztynowicz M, Dibarboure G, et al., 2016. Mesoscale resolution capability of altimetry: Present and future[J]. JOURNAL OF GEOPHYSICAL RESEARCH-OCEANS, 121(7): 4910-4927.

Fu L L, Pavelsky T, Cretaux J F, et al., 2024. The Surface Water and Ocean Topography Mission: A Breakthrough in Radar Remote Sensing of the Ocean and Land Surface Water[J]. GEOPHYSICAL RESEARCH LETTERS, 51(4): e2023GL107652.

He J, Xu Y, Sun H, et al., 2024. Sea Surface Height Wavenumber Spectrum from Airborne Interferometric Radar Altimeter[J]. REMOTE SENSING, 16(8): 1359.

Heslop E E, Sanchez-Roman A, Pascual A, et al., 2017. Sentinel-3A Views Ocean Variability More Accurately at Finer Resolution[J]. GEOPHYSICAL RESEARCH LETTERS, 44(24): 12367-12374.

Lapeyre G, Klein P, 2008. Dynamics of the Upper Oceanic Layers in Terms of Surface Quasigeostrophy Theory[J]. Journal of Physical Oceanography, 36(2): 165-176.

Le Traon P Y, Klein P, Hua B L, et al., 2008. Do altimeter wavenumber spectra agree with the interior or surface quasigeostrophic theory? [J]. JOURNAL OF PHYSICAL OCEANOGRAPHY, 38(5): 1137-1142.

Marks K M, Smith W H F, 2016. Detecting small seamounts in AltiKa repeat cycle data[J]. MARINE GEOPHYSICAL RESEARCH, 37(4): 349-359.

McWilliams, James C, 2016. Submesoscale currents in the ocean[J]. Proceedings. Mathematical, Physical, and Engineering Sciences / The Royal Society, 472(2189): 20160117.

Qiu B, Chen S, Klein P, et al., 2018. Seasonality in Transition Scale from Balanced to Unbalanced Motions in the World Ocean[J]. JOURNAL OF PHYSICAL OCEANOGRAPHY, 48(3): 591-605.

Qiu B, Nakano T , Chen S ,et al. Bi‐Directional Energy Cascades in the Pacific Ocean From Equator to Subarctic Gyre[J].Geophysical Research Letters, 2022(8):49.DOI:10.1029/2022GL097713.

Quartly G D, Passaro M, 2015. Initial Examination of AltiKa's Individual Echoes[J]. MARINE GEODESY, 38: 73-85.

Raynal M, Labroue S, Moreau T, et al., 2018. From conventional to Delay Doppler altimetry: A demonstration of continuity and improvements with the Cryosat-2 mission[J]. ADVANCES IN SPACE RESEARCH, 62(6): 1564-1575.

Richman J G , Arbic B K , Shriver J F ,et al.Inferring dynamics from the wavenumber spectra of an eddying global ocean model with embedded tides[J].Journal of Geophysical Research, C. Oceans: JGR, 2012(C12):117.DOI:10.1029/2012jc008364.

Rocha C B, Chereskin T K, Gille S T, et al., 2016. Mesoscale to Submesoscale Wavenumber Spectra in Drake Passage[J]. JOURNAL OF PHYSICAL OCEANOGRAPHY, 46(2): 601-620.

Samelson R M, Schlax M G, Chelton D B, 2014. Global observations of nonlinear mesoscale eddies (vol 91, pg 167, 2011) [J]. JOURNAL OF PHYSICAL OCEANOGRAPHY, 44(9): 2588-2589.

Smith K S, Vallis G K, 2001. The scales and equilibration of midocean eddies: Freely evolving flow[J]. JOURNAL OF PHYSICAL OCEANOGRAPHY, 31(2): 554-571.

Tchilibou, Michel, Gourdeau, et al. Spectral signatures of the tropical Pacific dynamics from model and altimetry: a focus on the meso-/submesoscale range[J].[2024-07-28].

Vergara O, Morrow R, Pujol I, et al., 2019. Revised Global Wave Number Spectra From Recent Altimeter Observations[J]. JOURNAL OF GEOPHYSICAL RESEARCH-OCEANS, 124(6): 3523-3537.

485   Vergara O, Morrow R, Pujol M I, et al., 2023. Global submesoscale diagnosis using along-track satellite
486   altimetry[J]. OCEAN SCIENCE, 19(2): 363-379.
487   Verron J, Bonnefond P, Andersen O, et al., 2021. The SARAL/AltiKa mission: A step forward to the
488   future of altimetry[J]. ADVANCES IN SPACE RESEARCH, 68(2): 808-828.
489   Verron J, Sengenes P, Lambin J, et al., 2015. The SARAL/AltiKa Altimetry Satellite Mission[J].
490   MARINE GEODESY, 38: 2-21.
491   Xu Y, Fu L L, 2011. Global Variability of the Wavenumber Spectrum of Oceanic Mesoscale
492   Turbulence[J]. JOURNAL OF PHYSICAL OCEANOGRAPHY, 41(4): 802-809.
493   Xu Y, Fu L L, 2012. The Effects of Altimeter Instrument Noise on the Estimation of the Wavenumber
494   Spectrum of Sea Surface Height[J]. JOURNAL OF PHYSICAL OCEANOGRAPHY, 42(12): 2229-
495   2233.
496   Yi J, Du Y, He Z, et al., 2014. Enhancing the accuracy of automatic eddy detection and the capability of
497   recognizing the multi-core structures from maps of sea level anomaly[J]. OCEAN SCIENCE, 10(1):
498   39-48.
499   ZHOU Run-sheng, ZHANG Sheng-jun, KONG Xiang-xue. Investigation on Along-Track Geoid
500   Resolution Capabilities of HY-2 Based on Spectrum Analysis[J]. Journal of Northeastern University
501   (Natural Science), 2023, 44(9): 1328-1336.